



**La₄Ni₃O_{10-δ} as an efficient solid oxide fuel cell cathode:
electrochemical properties versus microstructure**

Journal:	<i>Journal of Materials Chemistry A</i>
Manuscript ID	TA-ART-09-2015-007862
Article Type:	Paper
Date Submitted by the Author:	30-Sep-2015
Complete List of Authors:	Djurado, Elisabeth; LEPMI, Sharma, Rakesh; University of Grenoble, Lepmi Burriel, Monica; Laboratoire des Matériaux et du Génie Physique (LMGP),



Journal Name

ARTICLE

La₄Ni₃O_{10-δ} as an efficient solid oxide fuel cell cathode: electrochemical properties versus microstructureR. K. Sharma^{a, b}, M. Burriel^{c, d} and E. Djurado^{a, b}Received 00th January 20xx,
Accepted 00th January 20xx

DOI: 10.1039/x0xx00000x

www.rsc.org/

The higher-order Ruddlesden-Popper phase La₄Ni₃O_{10-δ} is prepared for the first time by electrostatic spray deposition (ESD) on CGO (Ce_{0.9}Gd_{0.1}O_{2-δ}) electrolyte and evaluated as Intermediate Temperature Solid Oxide Fuel Cell cathode. Different and innovative microstructures are obtained by varying the deposition time, nozzle to substrate distance, substrate temperature, solution flow rate, concentration and solvents. Single phase La₄Ni₃O_{10-δ} films crystallize in an orthorhombic layered Ruddlesden-Popper (*n*=3) structure after calcination at 950 °C for 8 h in air and is maintained after further sintering at 1100 °C for 6 h in air. The surface morphology, observed by SEM-FEG, is strongly influenced by the solution concentration, the nature of the solvents and the deposition temperature. The electrochemical properties are found to be strongly dependent on the microstructure of the cathode films. The lowest polarization resistance values obtained for the double layer (3-D coral-type film by ESD topped by a screen-printed layer) cathode are 2.01, 0.30 and 0.05 Ω.cm² at 600 °C, 700 °C and 800 °C, respectively. To the best of our knowledge, this La₄Ni₃O_{10-δ} cathode shows the best performance reported to date for this composition.

^a Univ. Grenoble Alpes, LEPMI, 1130 rue de la Piscine, BP 75, 38402 St Martin d'Hères Cedex, France.

^b CNRS, LEPMI, F-38000 Grenoble, France.

^c Catalonia Institute for Energy Research (IREC), Department of Advanced Materials for Energy, Jardins de les Dones de Negre 1, 2nd floor, 08930-Sant Adrià del Besòs, Barcelona, Spain

^d Univ. Grenoble Alpes, CNRS, LMGP, F-38000 Grenoble, France.

† Corresponding author, Phone: +33-476826684; Fax: +33-476826777; E-mail: elisabeth.djurado@lepmi.grenoble-inp.fr



Journal Name

ARTICLE

1. Introduction

The main objective of the current research on solid oxide fuel cells (SOFCs) is the lowering of the operating temperature from above 900 °C down to 700 °C (intermediate temperatures) in order to increase their lifetime and reduce the overall cost. However, the fuel cell performance degrades at lower temperature because of the larger overpotentials generated at the cathodic side and the larger ohmic losses in the electrolyte. Hence, the search for new mixed ionic-electronic conducting (MIEC) cathode materials is key, especially for improving the performance of Intermediate Temperature Solid Oxide Fuel Cells (IT-SOFCs) working at 500–700 °C.¹⁻⁵ The Ruddlesden-Popper (RP) family compounds with general formula ($\text{La}_{n+1}\text{Ni}_n\text{O}_{3n+1}$; $n=1, 2, 3$) have been suggested to be promising candidates for cathode materials [6-8]. The total conductivity of RP phases has been found to increase with n .^{6, 7, 9-11} In particular, the $\text{La}_3\text{Ni}_2\text{O}_{7.8}$ and $\text{La}_4\text{Ni}_3\text{O}_{10.8}$ compounds possess higher conductivity compared with $\text{La}_2\text{NiO}_{4+\delta}$ and also higher relative stabilities, which potentially could make them more suitable cathode materials for IT-SOFCs.^{6, 7, 12} As an example, the $\text{La}_4\text{Ni}_3\text{O}_{10.8}$ electrode performance of symmetrical cells with $\text{La}_9\text{Sr}_1\text{Ga}_8\text{Mg}_2\text{O}_{3.8}$ electrolyte was found the lowest one of the series ($1 \Omega \text{ cm}^2$ at 1073 K). Nickelates have also received much attention because they exhibit high kinetics with a surface exchange coefficient of $1.3 \times 10^{-7} \text{ cm.s}^{-1}$ measured at 700°C.¹³ Moreover, it is worth to mention that the thermal expansion coefficient of $\text{La}_4\text{Ni}_3\text{O}_{10.8}$ ($13.2 \times 10^{-6} \text{ K}^{-1}$) has been reported to be close to the common SOFC electrolyte materials such as the ceria based electrolytes (CGO) ($13.4 \times 10^{-6} \text{ K}^{-1}$) in air.⁶ The similar TEC values guarantees the thermo-mechanical compatibility between cell components.

Despite of the fact that several methods have been used for the synthesis of $\text{La}_4\text{Ni}_3\text{O}_{10.8}$: Pechini routes⁶, nitrate and citrate routes^{15, 16}, solid-state routes^{7, 17}, and continuous hydrothermal flow synthesis method¹⁸; the higher members of the $\text{La}_{n+1}\text{Ni}_n\text{O}_{3n+1}$ series, particularly $n=2$ and 3 are difficult to synthesize as a pure phase because they normally require prolonged homogenization and reheating procedures.^{6, 15, 17} For example Amow *et al.* prepared $\text{La}_4\text{Ni}_3\text{O}_{10.8}$ by the Pechini method at 1050 °C over 6 days with one intermittent regrinding step,^{6, 19} whereas Takahashi *et al.* synthesized $\text{La}_4\text{Ni}_3\text{O}_{10.8}$ by heating La_2O_3 and NiO at 1050 °C over 6 days with one intermittent regrinding step.⁷ Furthermore, Zhang *et al.* prepared the same composition by calcinations at 1100 °C for 4 ~ 5 days in air, also with several grinding processes.¹⁶

This article reports, for the first time, the facile preparation of pure $\text{La}_4\text{Ni}_3\text{O}_{10-\delta}$ films on CGO substrate by electrostatic spray deposition (ESD) followed by sintering in air. A systematic study of the effect of the ESD process parameters, such as deposition time, nozzle-to-substrate distance, substrate temperature, and the precursor solution, on the film microstructure is presented in order to optimize the $\text{La}_4\text{Ni}_3\text{O}_{10-\delta}$ electrode microstructure, required to improve the electrochemical performance. The electrochemical properties in air are investigated by electrochemical impedance spectroscopy (EIS) versus the microstructure for high performance IT-SOFCs applications.

2. Experimental

To prepare the solutions containing precursors with a La:Ni mole ratio of 4:3 stoichiometric amounts of nickel nitrate hexahydrate ($\text{Ni}(\text{NO}_3)_2 \cdot 6\text{H}_2\text{O}$, 99.9%, Aldrich) and lanthanum nitrate hexahydrate ($\text{La}(\text{NO}_3)_3 \cdot 6\text{H}_2\text{O}$, 99.9%, Alfa Aesar) were added to citric acid ($\text{C}_6\text{H}_8\text{O}_7$, 99.9%, Alfa Aesar) and ethanol ($\text{CH}_3\text{CH}_2\text{OH}$, >99.9%, prolabo, referred to as EtOH) into a 30 mL ethanol, ethanol-butyl carbitol ($\text{C}_4\text{H}_9(\text{OCH}_2\text{CH}_2)_2\text{OH}$, Acros Organics, 99+%, referred to as BC) (1:2), and ethanol-distilled water (1:2) solution with vigorous stirring over 3h. The total concentration of metal ions was varied from 0.005 M to 0.02M. The conductivity of each of the prepared solution was measured and is included in Table 1 together with the boiling points and surface tension.²⁰

Electrostatic spray deposition (ESD), with several advantages over conventional deposition techniques such as a simple set-up and the use of inexpensive precursors, has been used to deposit $\text{La}_4\text{Ni}_3\text{O}_{10-\delta}$ films on $\text{Ce}_{0.9}\text{Gd}_{0.1}\text{O}_{2-\delta}$ (CGO) substrates (~19 mm in diameter) in a vertical set-up configuration^{19, 21} under ambient atmosphere. ESD is based on electrohydrodynamic laws where a precursor solution is pumped through a metallic nozzle at a controlled flow rate. The solution is then atomized by applying a high voltage that generates an electrical field between the nozzle and the substrate. The electrical field generates the aerosol and directs it towards the substrate where the droplets spread, dry and decompose to form the film. The ESD raw coatings are amorphous. To crystallize the films a calcination step at 950 °C for 8 h in air was carried out after the deposition. The effect of the ESD process parameters (Table 2) such as deposition time, concentration, nature of the solvent, substrate temperature, nozzle to substrate distance and solution flow rate were investigated to control the film microstructure.

X-ray diffraction (XRD, Philips X'Pert-MPD system, Cu K_α radiation, $\lambda=1.54056 \text{ \AA}$) was used to determine the crystal structure. The phase identification was carried out using International Centre for Diffraction data (ICDD). The positions of X-ray diffraction peaks as well as the cell parameters were obtained by refinement using Fullprof software.²² Field emission scanning electron microscopy (ZEISS Ultra 55 instrument with field emission gun (FEG)) was used for the morphology evaluation of the film

surfaces and cross-sections and Energy-dispersive X-ray spectroscopy (EDX) for the composition analysis. Four symmetrical cells, cathode/ CGO electrolyte / cathode, were used for the electrochemical studies.

Ink for the screen-printing of the current collecting layer (CCL) was prepared using the KD2921 (Zschimmer and Schwarz) solvent and nickelate powder, previously synthesized by sintering (950 °C/ 8 h in air) of amorphous powder obtained by the heating of the ESD precursor solution at 150 °C. For the double layer cathode, the $\text{La}_4\text{Ni}_3\text{O}_{10-\delta}$ -based CCL was screen printed (SP) on the ESD films deposited on the CGO electrolyte (see Table 3) and then sintered under air at 1050 °C for 2h followed by 1100 °C for 0.5 h. The cathode area of each ESD prepared cathode was of 2.0 cm² whereas for the double layer (ESD + SP) of 1.54 cm². Electrochemical Impedance Spectroscopy (EIS) measurements were carried out with a PARSTAT 302N in a symmetrical two-electrode configuration in air between 500 and 800 °C. The measurements were performed in the frequency range from 50 mHz to 100 kHz with signal amplitude of 0.02 V at open-circuit voltage, using Au grids (Heraeus, 1024 meshes/cm² woven from 0.06 mm dia. wire) as current collectors. The impedance diagrams were fitted to equivalent circuits using the ZView[®] software (Scribner Associates).

Table 1. Solvent composition, concentration, conductivity, boiling points and surface tensions of the precursor solutions.²⁰

Solutions	Solvent(s)	Solution concentration (mol·L ⁻¹)	Solution conductivity (mS·cm ⁻¹)	Boiling point (°C)	Surface tension (mN·m ⁻¹)
S _A	EtOH + BC (1:2)	0.02	0.06	168	27
S _B	EtOH, 100 %	0.005	0.16	78	21
S _C	EtOH, 100 %	0.01	0.19	78	21
S _D	EtOH, 100 %	0.02	0.26	78	21
S _E	EtOH + H ₂ O (1:2)	0.02	3.34	93	55

Table 2. ESD process parameters investigated to control the film microstructure.

Process parameters	Substrate temperature [°C]	Deposition time [h]	Flow rate [mL.h ⁻¹]	Nozzle-to-substrate distance [mm]	Nature of solvent(s)	Solution concentration[M]
Deposition time	350	0.5 1.5 2.0 3.0	1.5	50	EtOH	0.02
Solution concentration	350	3.0	1.5	50	EtOH	0.005 0.01 0.02
Nature of solvent(s)	350	3.0	1.5	50	EtOH EtOH:H ₂ O, 1:2 EtOH:BC, 1:2	0.02
Substrate temperature	300 350 400	3.0	1.5	50	EtOH:H ₂ O, 1:2	0.02
Nozzle-to-substrate distance	350	3.0	1.5	30 50	EtOH:H ₂ O, 1:2	0.02

3. Results and discussion

3.1. Structural characterization and elemental analysis

Figure 1 shows the FULLPROF refinement of La₄Ni₃O_{10-δ} film deposited on CGO at 350°C and calcined at 950 °C/ 8 h + 1100 °C/ 6 h in air. All the films crystallize in a pure orthorhombic cell regardless of the sintering conditions: (i) at 950 °C for 8 h in air, (ii) at 950 °C for 8 h in air followed by sintering of 1100 °C for 6 h in air. No impurities or secondary phases can be observed even after the second calcination at 1100°C. All diffraction peaks matched well those of La₄Ni₃O_{10-δ} phase (ICDS #04-009-2594) and were indexed to an orthorhombic unit cell with the Fmmm space group (N° 69). The cell parameters of $a = 5.413(2) \text{ \AA}$, $b = 5.462(3) \text{ \AA}$ and $c = 27.960(5) \text{ \AA}$, deduced from Fullprof software refinement, are found to be in good agreement with previously reported values.^{6, 15, 17} The EDX spectrum, shown in Fig 2, confirmed the presence of La, Ni and O elements in the film with a La/Ni ratio of 1.28 ± 0.05 , as expected.

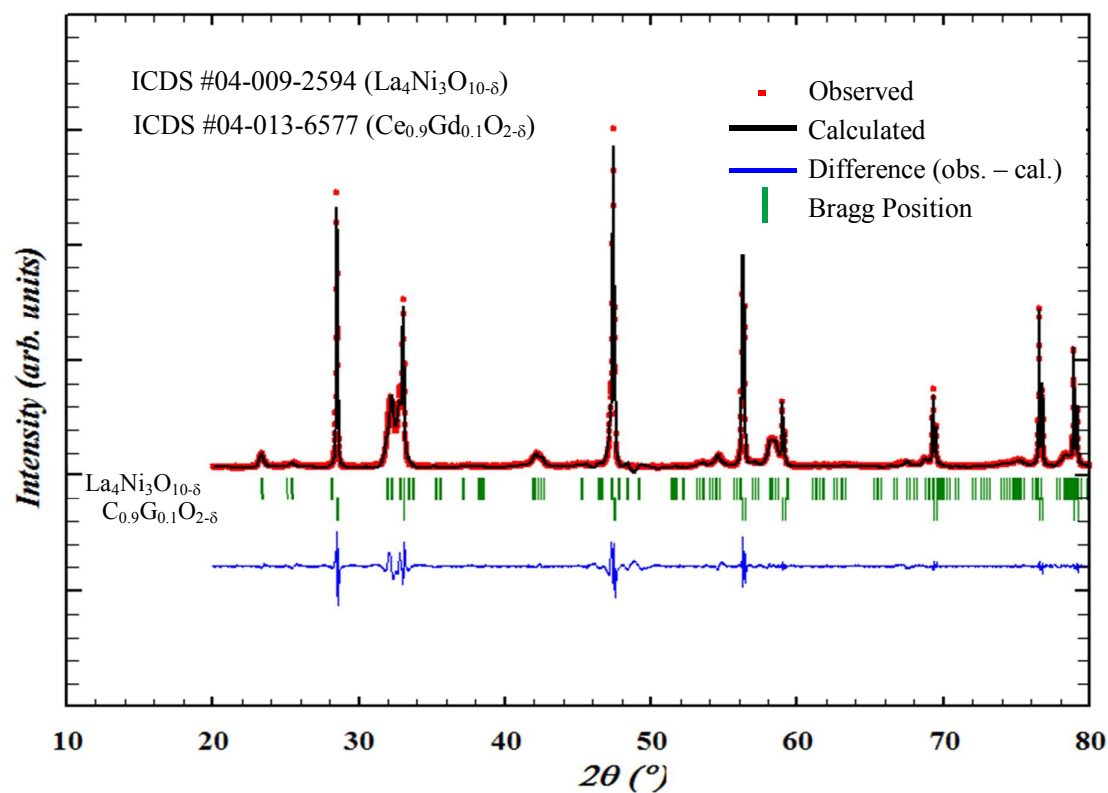


Fig. 1. FULLPROF refinement of the XRD pattern of $\text{La}_4\text{Ni}_3\text{O}_{10-\delta}$ film deposited by ESD at 350°C on a CGO substrate and after calcination at $950^\circ\text{C}/8\text{ h} + 1100^\circ\text{C}/6\text{ h}$ in air.

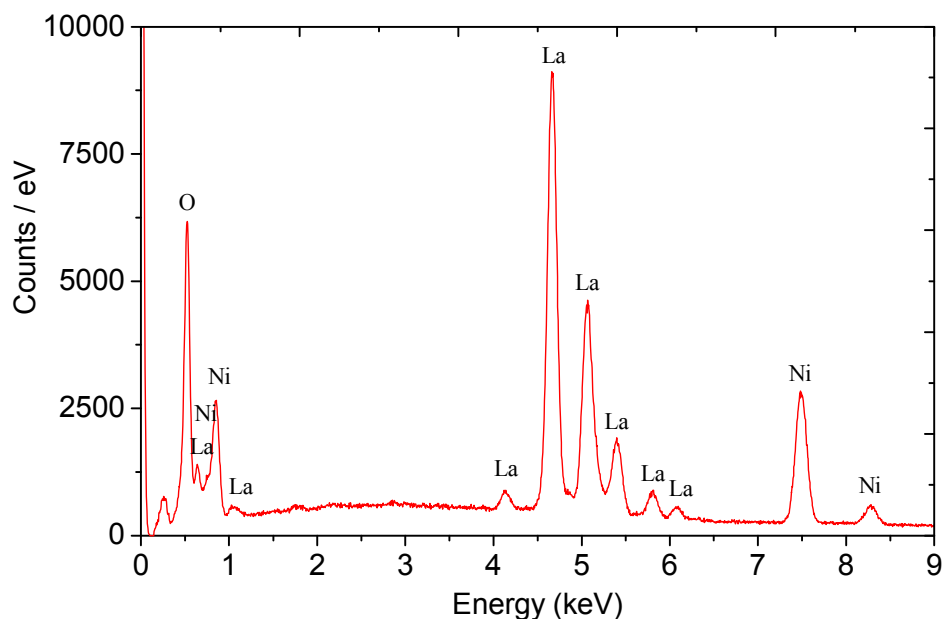


Fig.2. Typical EDX spectrum of the $\text{La}_4\text{Ni}_3\text{O}_{10-\delta}$ film calcined at 950 °C for 8 h in air

3.2. Microstructural characterization

In a first step, ESD was systematically investigated for the preparation of various microstructures depending on five process parameters (see Table 2). The microstructure of the film deposited by this technique highly depends on the size of the droplets impacting the heated substrate. The droplet size is determined by the substrate temperature, the droplet flight time between the needle and the substrate during transport of the aerosol spray, and the precursor solution flow rate. Therefore the size of the droplets can be easily tuned in a controlled manner by changing the deposition parameters. Several studies have modelled how the solution properties and the deposition parameters determine the droplet size formed at the nozzle,^{23,24} being the Gañan-Calvo's relationship the most consensual one²⁵:

$$d \sim \left(\frac{\rho \varepsilon_0 Q^3}{\gamma K} \right)^{1/6} \quad (\text{Equation 1})$$

where d is the droplet diameter, ρ the density, ε_0 the vacuum permeability, Q the flow rate, γ the surface tension and K the electrical conductivity of the solution.

3.2.1. Influence of the deposition time

To study the evolution of the film growth and microstructure, $\text{La}_4\text{Ni}_3\text{O}_{10-\delta}$ films have been prepared at 350 °C varying the deposition time from 0.5 to 3 h while maintaining a pure EtOH solution, a nozzle to substrate distance of 50 mm, a flow rate of 1.5 mL/h and a concentration of the precursor solution of 0.02 M (see Table 2). A significant evolution of the surface morphology is evidenced over time (Fig. 3), especially between 0.5 h (Fig. 3-c) and 1.5 h (Fig. 3-f). As the deposition time was raised, an increase in particle agglomeration resulted from preferential landing of the aerosol droplets and from the lack of wetting on the substrate²⁶ due to the nearly dry aerosol droplets. With increasing time, a larger number of droplets arrive on the substrate changing the smooth surface of the original substrate and creating some irregularities with higher curvature. The charges on the substrate surface induced by the strong applied electrostatic field concentrate more where the curvature is greater.²⁷ So the charged droplets arriving at the surface will be more attracted towards these more curved areas. This is referred to as “preferential landing”. This action will cause particle agglomeration, especially when the droplets are small and light. Hwang *et al.*²⁷ have shown that when the substrate roughness is increased, preferential landing is promoted leading to particle agglomeration. In our case, several agglomerates are clearly visible after 0.5 h of deposition due to the preferential attraction (Fig. 3a) and this agglomeration increases with increasing time as shown in Fig. 3d, 3g and 3j. The thickness was found to be about 6 μm in average after 0.5 h (Fig. 3c), 15 μm after 1.5 h (Fig. 3f), 18 μm after 2 h (Fig. 3i) and 26 μm after 3 h (Fig. 3l).

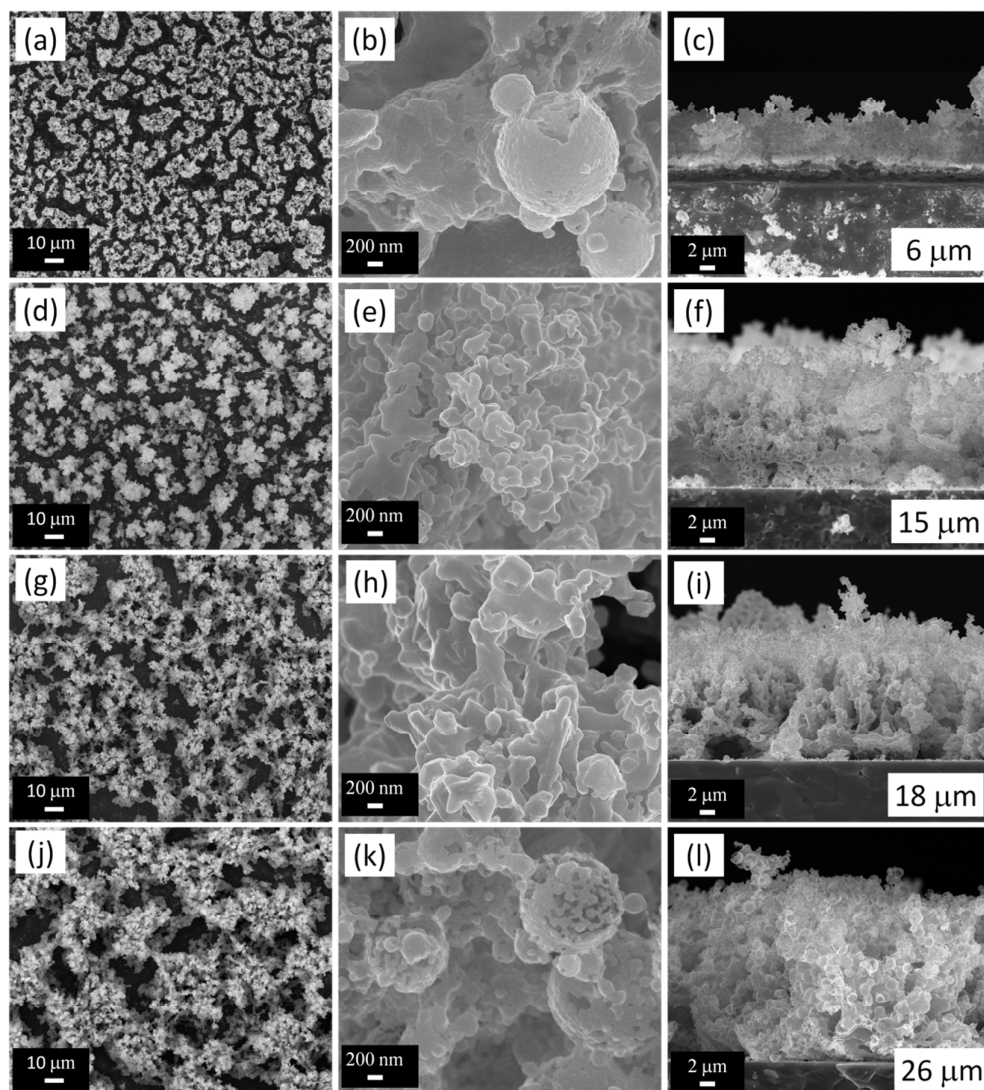


Fig. 3. SEM micrographs of the calcined (950°C for 8 h in air) ESD films using EtOH and 0.02 M salt concentration at $T=350\text{ }^{\circ}\text{C}$, for a distance nozzle to substrate of 50 mm and a flow rate of $1.5\text{ mL}\cdot\text{h}^{-1}$ after deposition time of: 0.5 h (a, b) surface, (c) cross section; 1.5 h (d, e) surface, (f) cross section; 2 h (g, h) surface, (i) cross section; 3 h (j, k) surface, (l) cross section.

3.2.2. Influence of the precursor solution concentration

The influence of the precursor concentration on the film morphology was studied for different salt concentrations of 0.005, 0.01 and 0.02 M (Figure 4). The other ESD deposition parameters were maintained constant at a flow rate of $1.5\text{ mL}\cdot\text{h}^{-1}$, substrate temperature of $350\text{ }^{\circ}\text{C}$, 3 h deposition time, nozzle-to-substrate distance equal to 50 mm and using pure ethanol as the solvent (see Table 2). The measured electrical conductivity of the precursor solution decreases with the precursor concentration as

shown in Table 1, in good agreement with previous observations.¹¹ Having considered capillary equilibrium, liquid continuity and moment and charge continuity at the jet, Gañan-Calvo deduced the following relation for polar liquids:

$$d \sim \epsilon_r^{1/6} \left(\frac{Q}{K} \right)^{1/3} \text{ (Equation 2)}$$

where ϵ_r , d and Q are the relative permittivity of the solution, the diameter of the droplets emitted at the jet (the primary droplet size) and the flow rate of the solution, respectively. As a result, the primary droplet size depends on these 3 parameters. Thus for a given flow rate (in this case, $1.5 \text{ mL}\cdot\text{h}^{-1}$), the droplet size depends only on the conductivity of the solution provided that the permittivity of the solution is kept constant. For the ethanol solution, the permittivity is approximately $2 \times 10^{-10} \text{ F m}^{-1}$.²⁰

As evidenced in Fig. 4a-d, a similar “cauliflower” like microstructure has been observed for the solution of concentration 0.005 and 0.01 M. Since the conductivity of the solution is quite similar (Table 1), a closed morphology with primary particle size of $\sim 100 \text{ nm}$ can be observed. When the concentration of the solution is increased to 0.02 M, some large, very porous and connected agglomerates are visible (Fig. 4e, 4f). These round-shape agglomerates consist of finer particles of an approx. 50 nm diameter size. According to equation 2, a higher concentration and hence a higher conductivity (passing to $0.26 \text{ mS}\cdot\text{cm}^{-1}$) will result in a smaller droplet size. They are smaller and lighter so their movement direction can be changed considerably by the attraction of induced charges at the substrate surface to form agglomerates.

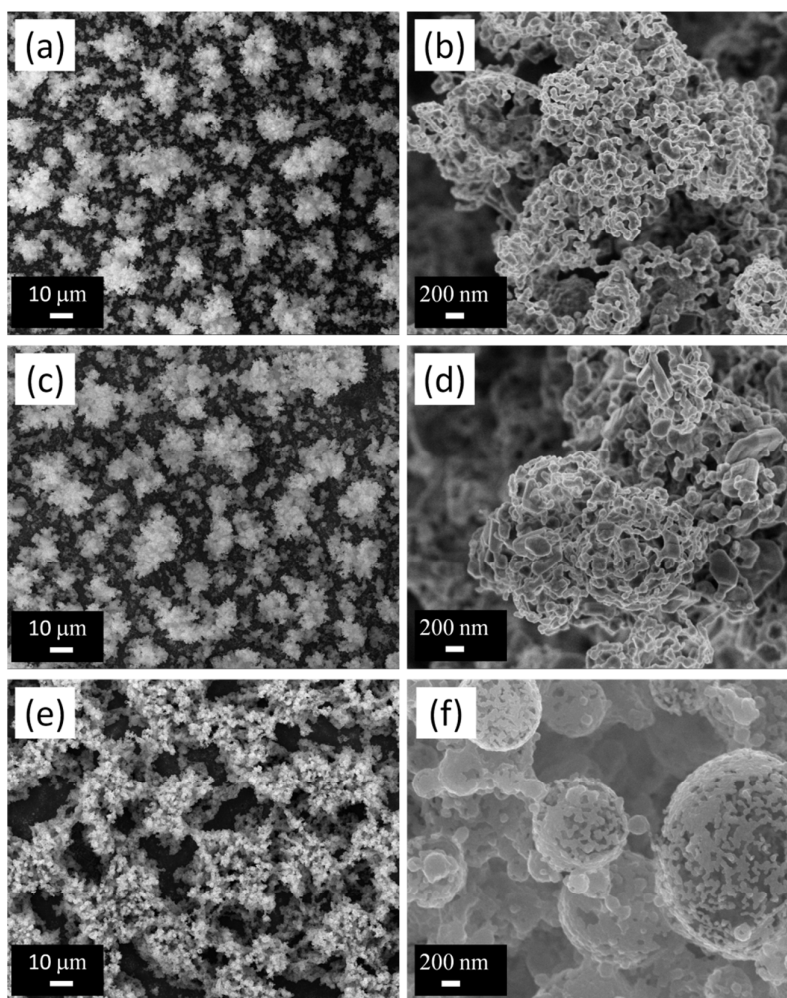


Fig.4. SEM surface micrographs (at 2 different magnifications) of calcined (950 °C for 8 h in air) $\text{La}_4\text{Ni}_3\text{O}_{10-\delta}$ ESD films obtained with a solution concentration of (a), (b) 0.005 M; (c) (d) 0.01 M; (e), (f) 0.02 M, using pure EtOH at $T=350$ °C for a nozzle to substrate distance of 50 mm and a flow rate of $1.5 \text{ mL}\cdot\text{h}^{-1}$ and after deposition time of 3 h.

3.2.3. Influence of the solvent composition

The physico-chemical properties of the precursor solution also play an important role in the ESD process and especially on the droplet size, which determines the morphology of the coating. In particular, the boiling point, conductivity and surface tension are crucial factors affecting both the evaporation of the solvents during the transport and the spreading of the droplets that impact the substrate. By changing the solvent composition, the layer morphology may also be modified. At a fixed optimized concentration of 0.02 M three different solvent compositions of EtOH: BC(1:2), EtOH 100% and EtOH: water (1:2), referred to as S_A , S_D and S_E (Table 1) have been selected to study their effect on the evolution of the

La₄Ni₃O_{10-δ} film morphology. In this study, the other process parameters: substrate temperature, solution flow rate, nozzle-to-substrate distance and deposition time were fixed at 350 °C, 1.5 mL.h⁻¹, 50 mm and 3h, respectively (Table 2). The resulting microstructures are shown in Fig. 5. A larger particle size (~200 nm) can be observed (Fig. 5a, 5b) when BC is added to EtOH (S_A) in comparison to our previous investigation with S_D (Fig. 5c, 5d) (~50 nm). According to equation 1, since the conductivity has been drastically reduced to 0.06 mS.cm⁻¹ and the surface tension is of the same order of magnitude (Table 1), the droplet size is expected to be larger in S_A, being mainly proportional to K^{-1/6}. These larger particles also originate from the higher boiling point of the EtOH:BC (1:2) solution (S_A, Table 1). Considering that the evaporation rate for S_A is slower than that of S_D (pure EtOH), a slower drying process is expected. The large liquid droplets of S_A are expected to spread much more on the heated substrate than the smaller and drier droplets of S_D. Consequently, the coating obtained from S_A (Fig. 5a, 5b) presents a porous connected net with larger particles than the net of round shape agglomerates with finer grains in S_D (Fig. 5c, 5d). The addition of H₂O in EtOH (S_E) leads to a higher conductivity of the precursor solution and larger surface tension (Table 1) than in S_D and S_A and, consequently, to a decrease in the droplet size (see Equation 1). However, the particle size observed in Figures 5e and 5f (150 nm) is not as small as the one in S_D (50 nm, Fig. 5d). Indeed, we also have to consider the boiling point of S_E which is larger than in the case of S_D (93 °C against 78 °C, Table 1). This is the factor which is countering the effect of conductivity and surface tension parameters and may lead to intermediate final particle sizes (~150 nm) for S_E (Fig. 5f). In these conditions, a porous reticulation is observed with particle size ranging from ~200 nm (S_A) (Fig. 5b), ~ 50 nm (S_D) (Fig. 5d) and ~ 150 nm (S_E) (Fig. 5f).

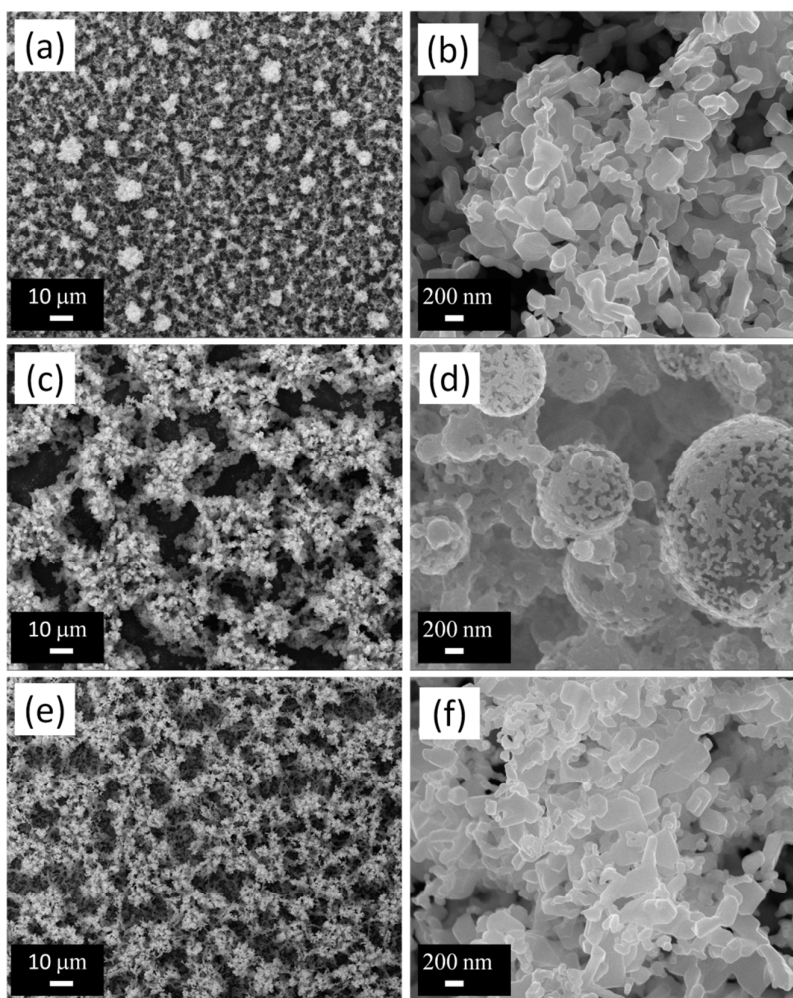


Fig. 5. SEM surface micrographs (at 2 different magnifications) of calcined (950 °C for 8 h in air) $\text{La}_4\text{Ni}_3\text{O}_{10-\delta}$ ESD films obtained with solution of (a), (b) S_A : EtOH + BC (1:2); (c), (d) S_D : EtOH; (e), (f) S_E : EtOH + H_2O (1:2) with a solution concentration of 0.02 M at $T=350$ °C for a nozzle to substrate distance of 50 mm and a flow rate of $1.5 \text{ mL}\cdot\text{h}^{-1}$ and after deposition time of 3 h.

3.2.4. Influence of the substrate temperature

The substrate deposition temperature has been reported to be a main parameter, since the entire pyrolysis processes take place at or near the substrate surface.²⁸ The temperature plays a role in conditioning the drying rate of the droplets during the flight, the rate at which they dry once deposited on the substrate, the way in which the droplets spread on the surface have an effect in the resulting microstructure. As observed by Nguyen *et al.*²⁹, a mere 5 °C difference is sufficient to modify the droplet size and thus, to radically change the resulting microstructure. For the solution S_E , the evolution of the surface microstructure of the $\text{La}_4\text{Ni}_3\text{O}_{10-\delta}$ films deposited at different temperatures ranging from 300 °C to 400 °C

is shown in Fig. 6. The precursor solution concentration, nozzle-to-substrate distance, flow rate and deposition time were fixed at 0.02 M, 50 mm, 1.50 mL.h⁻¹ and 3 h, respectively. At 300 °C, cracks have been observed (Fig. 6a) which could be due to stresses developed during the drying process of a large quantity of liquid present on the substrate at this low temperature. When large droplets impact the heated substrate, simultaneous spreading and drying processes occurs. Consequently, large particles of approx. 100 x 400 nm are obtained. As the deposition temperature was raised to 350 °C, the arriving droplets contained less solvent. Therefore the drying step is more homogeneous and smaller connected particles of ~ 150 nm are visible. The cracks disappeared and a porous reticulated La₄Ni₃O_{10-δ} film is observed. An increase in particle agglomeration (Fig. 6c) resulted from preferential landing of the aerosol droplets and from the lack of wetting on the substrate²⁶ due to the nearly dry aerosol droplets. At higher temperatures drier particles arrive on the substrate changing the surface of the original substrate and creating some irregularities with higher curvature. On further increasing the temperature to 400 °C, no change in the particle size has been observed (Fig. 6d and 6e).

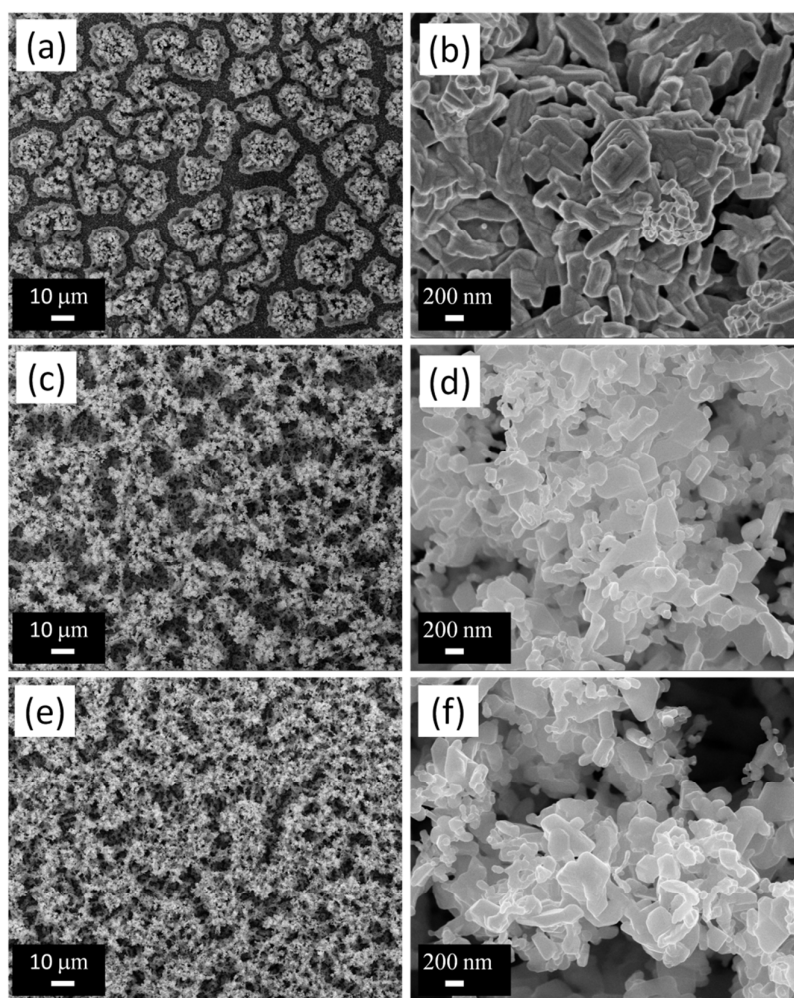


Fig.6. SEM surface micrographs (at two different magnifications) of calcined (950°C for 8 h in air) $\text{La}_4\text{Ni}_3\text{O}_{10-\delta}$ films obtained by ESD at deposition temperatures of: (a), (b) 300°C ; (c), (d) 350°C ; (e), (f) 400°C with a solution concentration of 0.02 M for a nozzle to substrate distance of 50 mm and a flow rate of $1.5\text{ mL}\cdot\text{h}^{-1}$ and after deposition time of 3 h.

3.2.5. Effect of the nozzle to substrate distance

The amount of precursor solution arriving onto the substrate is also controlled by the nozzle to substrate distance. The shorter the distance, the larger the amount of precursor solution deposited. Therefore we could expect to control the film porosity by changing the nozzle to substrate distance in the same way as the influence of temperature in terms of quantity of solution arriving on the substrate. Figure 7 shows surface morphologies of $\text{La}_4\text{Ni}_3\text{O}_{10-\delta}$ films deposited at two different nozzle-to-substrate distances of 30 and 50 mm using solution S_E (Tables 1 and 2). The solution flow rate, substrate temperature and total deposition time were fixed at $1.5\text{ mL}\cdot\text{h}^{-1}$, 350°C and 3 h, respectively. The reticulated microstructures of

the films deposited at 30 and 50 mm are quite similar but are composed of nanostructured particles of ~ 200 nm at only 30 mm and slightly smaller, ~ 150 nm for 50 mm (Fig. 7a-b and 7c-d, respectively). As the nozzle to substrate distance increases, it takes a longer time for the droplets to reach the substrate, allowing for a greater solvent evaporation and resulting in drier and smaller droplets when impacting the substrate. In both cases a 3-D coral-type microstructure has been obtained with a slightly more porous microstructure at 50 mm, with smaller connected particles.

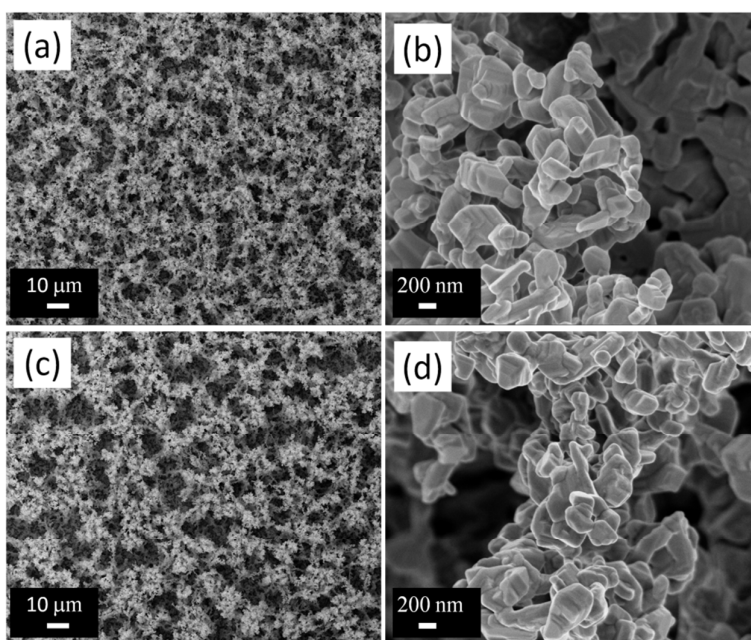


Fig. 7. SEM surface micrographs (at 2 different magnifications) of the calcined (950°C for 8 h in air) $\text{La}_4\text{Ni}_3\text{O}_{10-\delta}$ films obtained at a deposition temperature of 350°C , a deposition time of 3 h, a flow rate of $1.5\text{ mL}\cdot\text{h}^{-1}$ and a nozzle to substrate distance of: (a), (b) 30 mm; (c), (d) 50 mm with a S_E solution of concentration 0.02 M.

3.2.6. Selected $\text{La}_4\text{Ni}_3\text{O}_{10-\delta}$ films microstructures for electrochemistry

The electrochemical properties of the oxygen electrodes depend on their microstructure (percolation path between grains, particle size, porosity), on the electrolyte-electrode interface contact for oxygen ion transfer and on the current collection, to enhance the electronic conductivity. In order to study the effect of the $\text{La}_4\text{Ni}_3\text{O}_{10-\delta}$ films microstructure on their electrochemical properties, we have selected three ESD film microstructures, which differ qualitatively in terms of the percolation path inside the electrode and of the quality of the contact at the $\text{La}_4\text{Ni}_3\text{O}_{10-\delta}$ / CGO interface. These specimens consist of “isolated cauliflowers” (sample 1, Fig. 8a-b), connected round agglomerates (sample 2, Fig. 8d-e) and 3D coral-

type microstructure (sample 3, Fig. 8g-h). The films were deposited at a substrate temperature, nozzle to substrate distance, flow rate and deposition time of, 350 °C, 50 mm, 1.5 mL.h⁻¹ and 3h, respectively. The other ESD parameters such as nature of the solvents and concentration of the precursor solution used for such microstructures are given in Table 3, along with some characteristics of the microstructure. The porosity of the films was estimated by comparing the apparent film density with the La₄Ni₃O_{10-δ} theoretical density. The apparent density was obtained by weighing the CGO substrates before and after the ESD film deposition and measuring the average film thickness and diameter. A porosity of approximately 95, 92 and 86 vol. % was estimated for the isolated cauliflower, connected round agglomerates and 3-D coral type microstructures, respectively. This large porosity indicates that plenty of space is available for oxygen molecules to transport in ESD film. These values are in good agreement with the porosity reported by Sar et. al. using FIB-SEM on the CGO/La_{0.6}Sr_{0.4}Co_{0.2}Fe_{0.8}O_{3-δ} film also deposited by ESD.³⁰ Further all three electrodes are characterized by an average particle size varying from 50 nm (sample 2, Fig. 4f), to 100 nm (sample 1, Fig. 4d) to 150 nm (sample 3, Fig. 5f) with a difference in percolation and in the presence or absence of a continuous thin dense cathode layer between the electrolyte and the porous cathode. It is obvious from Fig. 8c and 8f that samples 1 and 2 do not have the continuous thin dense layer, whereas sample 3 (3D coral-type microstructure) and sample 4 (3D coral-type microstructure topped by SP layer) do present a continuous and adherent interface (Fig. 8i). The origin of this thin dense layer is the lower evaporation rate and larger amount of the liquid in the charged droplet of EtOH + water (1:2) based precursor solution (used for samples 3 and 4) in comparison to the finer and almost dry droplets of the EtOH based solution (used for samples 1 and 2). As a consequence, the charged liquid droplets containing water, spread much more on the polished flat surface of the grounded substrate than a finer droplets containing EtOH. This leads to the formation of a continuous thin dense layer also improving the adherence of the electrode-electrolyte interface without the need of using high sintering temperatures. In these conditions, one can notice that ESD is the unique process able to deposit a thin dense layer with an active electrode in one step. Clearly, the percolation path in sample 2, composed of connected round agglomerates, is better than that of the isolated cauliflowers (sample 1). The percolation path is further improved for sample 3, with a 3-D coral-type microstructure. In order to further improve the lateral percolation and to ensure a better contact between the current collecting grid and the cathode, a double layer cathode (sample 4, Fig. 8j) was prepared by screen-printing (SP) a 20 μm thick current collecting layer of La₄Ni₃O_{10-δ} on the top of the functional 3-D coral cathode (20 μm thick) (Fig.8g and 8h). As shown in Fig.8k, the screen-printed layer with primary particle size of 600 nm is partially penetrating the ESD functional layer in a depth of approximately 10μm. The total double layer thickness is 30 μm.

Table 3. Sample, microstructure, ESD coating conditions, sintering conditions (in air) and cathode thickness and particle size of the selected films for electrochemical measurements.

Samples	Microstructure	Nature of solvent(s)	Concentration of solution(s)	Flow rate [mL.h ⁻¹]	Sintering Temperature [°C]	Thickness of the cathode [μm]	Particle size [nm]
Sample 1	Isolated cauliflowers	S _C	0.01	1.5	950/ 8h	38	100
Sample 2	Connected round agglomerates	S _D	0.02	1.5	950/ 8h	26	50
Sample 3	3-D coral-type	S _E	0.02	1.5	950/ 8h	24	150
Sample 4	Double layer (3-D coral-type + SP)	S _E	0.02	1.5	950/ 8h 1050/ 2h+ 1100/ 0.5h	30	150 (ESD), 600 (SP)

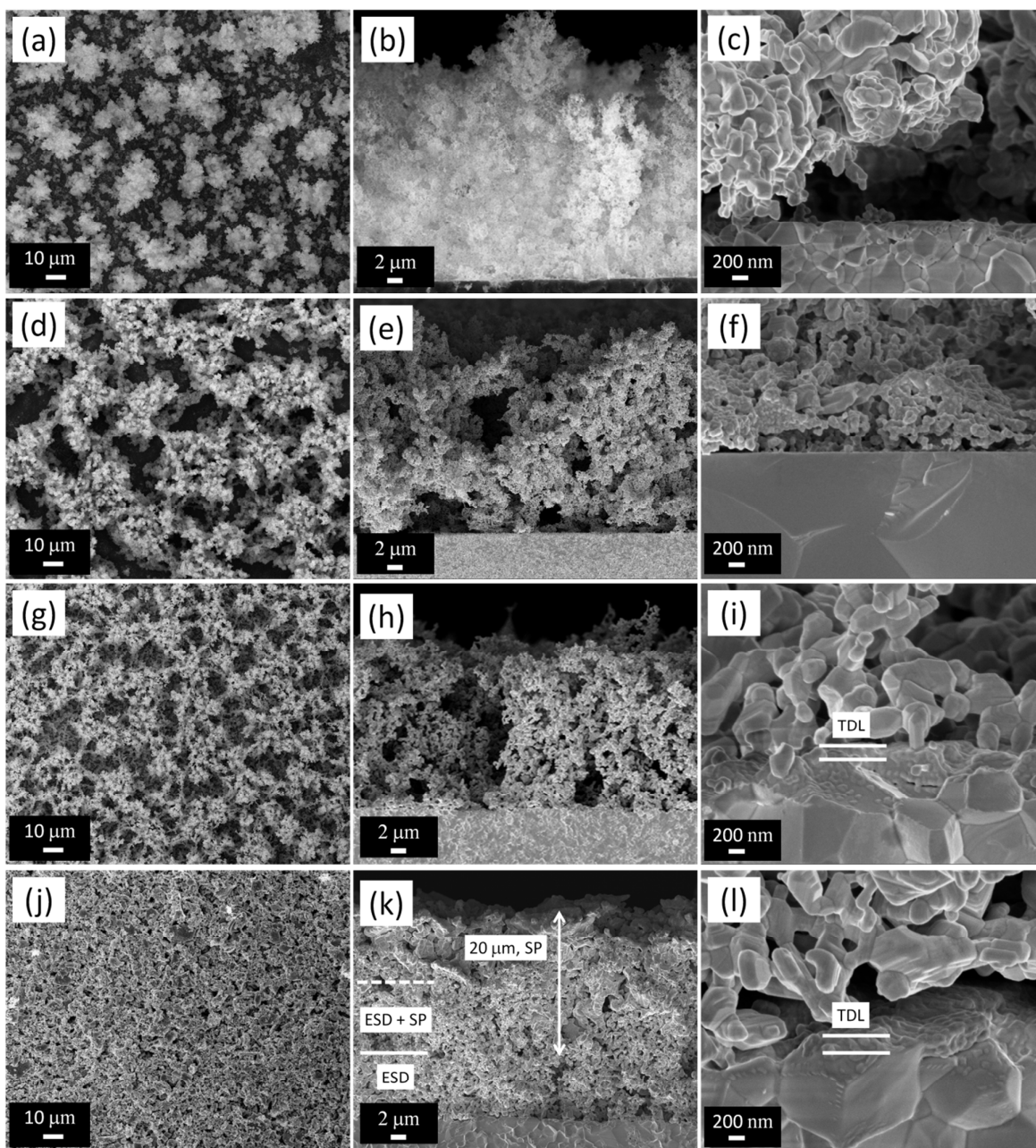


Fig.8. SEM micrographs of the $\text{La}_4\text{Ni}_3\text{O}_{10-\delta}$ cathode, sample 1: (a) surface, (b) cross section, (c) cross section of a selected region with discontinuous interface; sample 2: (d) surface, (e) cross section, (f) cross section of a selected region with discontinuous interface; sample 3: (g) surface, (h) cross section, (i) interface with a thin dense layer (TDL); sample 4 (double layer cathode (ESD + SP)): (j) surface (k) cross section, (l) interface with a thin dense layer (TDL). Samples 1-3 were calcined at 950 °C for 8 h in air whereas sample 4 at 950 °C for 8 h (after ESD) + 1050 °C for 2 h + 1100 °C for 0.5 h (after SP in air).

3.3. Electrochemical properties

The electrochemical properties of the four selected $\text{La}_4\text{Ni}_3\text{O}_{10-\delta}$ electrodes (samples 1-4, Table 3) deposited as symmetrical cells on CGO were investigated by EIS in air between 500 and 800 °C at open circuit potential (OCP). Fig. 9 shows the impedance spectra of the four selected cathodes at 700°C presented on a Nyquist plot and Fig. 10 shows the equivalent electrical circuit model used to fit the impedance spectra. All experimental diagrams were fitted using a series combination of two resistance-constant phase element parallel circuits ($R1//CPE1$ at high frequency, $HF / (LF$ for sample 4), and $R2//CPE2$ at low frequency, $LF /$ (very low frequency for sample 4)) connected in series with an inductance $L1$ and with series resistance R_s . The HF intercept of the diagrams on the real axis corresponds to the overall ohmic resistances (R_s , Table 4), including the resistive contributions of the electrolyte, electrode, leads, cathode and electrolyte interface and contact between electrode and grid. At 700 °C, R_s decreases from 31.97 $\Omega\cdot\text{cm}^2$ (sample 1), to 20.73 and 17.78 $\Omega\cdot\text{cm}^2$ (samples 2 and 3, respectively) (Fig. 9). This significant variation in R_s from sample 1 to sample 2 can be attributed to an improved contact between the electrode and the current collecting grid (surface view, Fig 8a compared to Fig. 8d). From samples 2 to 3 the contact at electrolyte/electrode interface improves, increasing the number of contact points between the cathode and the electrolyte (Fig 8i compared to Fig. 8f) due to the presence of a continuous thin dense layer. Indeed in the cases of sample 2 and 3, the constriction effect of the current lines is lowered since the contact between electrode and grid as well as interface between electrolyte and electrode both are better in comparison to sample 1 characterized by isolated cauliflowers. As we can see in Fig. 8c and 8f, samples 1 and 2 do not have continuous thin dense layer of cathode between the electrolyte and cathode, as is the case for sample 3 and sample 4 (Fig. 8i and 8l). A much lower R_s value could be expected for sample 3 in comparison sample 2 due to better contact of electrode with electrolyte at the interface (presence of thin dense layer, Fig.8l), however it is not found due to the poor contact between the electrode and the grid and hence to poor current collection (Fig. 8g). A clear reduction of R_s down to 3.43 $\Omega\cdot\text{cm}^2$ (sample 4, Table 4, Fig. 9d) is obtained when the ESD coral-type film is topped by a SP $\text{La}_4\text{Ni}_3\text{O}_{10-\delta}$ layer. This SP layer leads to a flatter electrode surface (Fig. 8j) and hence to a better contact resulting in a better current collection. This means that SP $\text{La}_4\text{Ni}_3\text{O}_{10-\delta}$ layer acts as a current collector layer (CCL). The polarization resistance (R_{pol}) which is used to quantify the magnitude of the electrode reaction, is defined as

$$R_{\text{pol}} = R_{\text{electrode}} \times S/2$$

where $R_{\text{electrode}}$ is the resistance difference measured between the value of the low frequency intercept of the electrode characteristic on the real axis and R_s . The surface area of each symmetrical electrode is

referred to as S and given in Table 4. According to the analysis, all electrode responses (samples 1-3) can be separated into two arcs (*HF* and *LF* ones respectively). The *HF* contribution is usually attributed to the charge transfer from the electrode to the electrolyte while the *LF* one is associated with the diffusion resistance, including the adsorption-desorption of oxygen, oxygen diffusion at the gas-cathode interface, and the surface diffusion of intermediate oxygen species.³¹

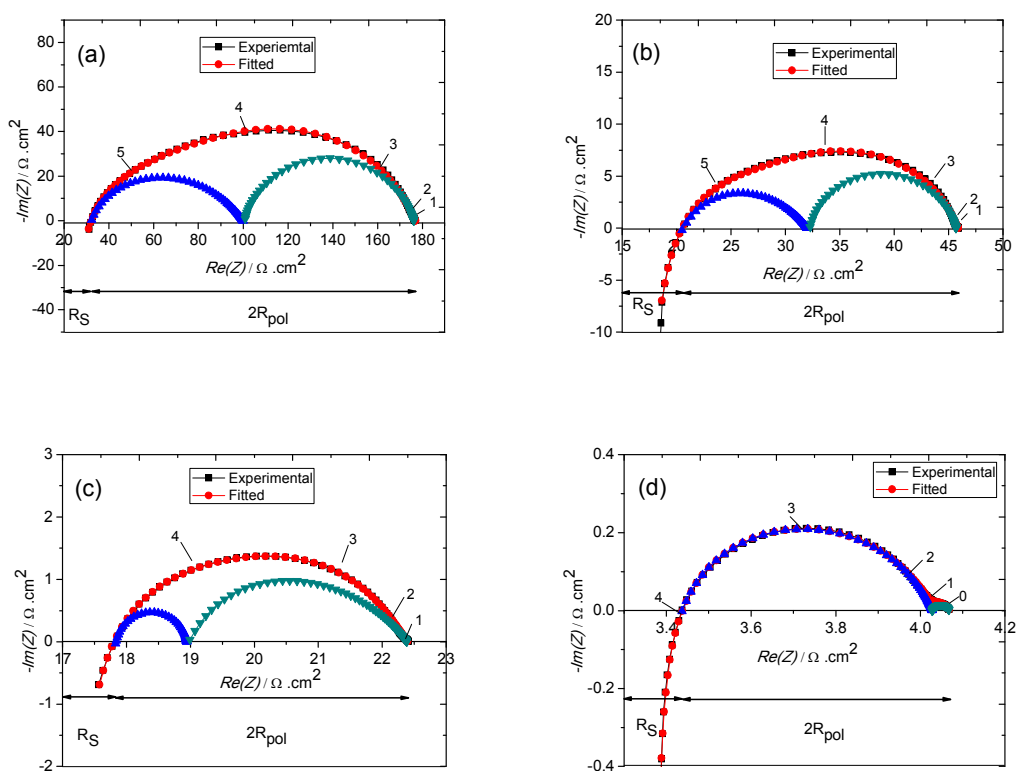


Fig. 9. Nyquist plots for the $\text{La}_4\text{Ni}_3\text{O}_{10-\delta}/\text{CGO}/\text{La}_4\text{Ni}_3\text{O}_{10-\delta}$ cells with different microstructure recorded in air at 700°C in OCP conditions: (a) sample 1 (b) sample 2 (c) sample 3 (d) sample 4. The numbers over the diagram indicate the logarithm of the measuring frequency.

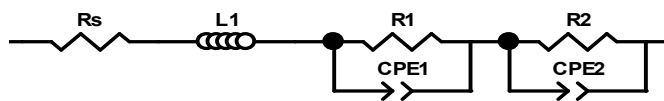


Fig. 10. Equivalent electrical circuit model used for impedance spectra fitting.

Table 4. Microstructures, surface area (S), series resistance (R_s), polarization resistance (R_{pol}) and activation energy (E_a) values in air for the 4 investigated samples.

Samples	Microstructure	Surface area [cm ²]	R_s at 700 °C [Ω cm ²]	R_{pol} at 700 °C [Ω cm ²]	R_{pol} at 800 °C [Ω cm ²]	E_a [eV]
Sample 1	Isolated cauliflowers	2.00	31.97	72.41	18.86	1.16
Sample 2	Connected round agglomerates	2.00	20.73	12.78	4.20	0.91
Sample 3	3-D coral-type	2.00	17.78	2.21	0.84	0.72
Sample 4	Double layer (3-D coral-type + SP)	1.54	3.43	0.30	0.05	1.32

Regardless of electrode microstructure, R_{pol} decreases by improving the percolation of the isolated cauliflowers (from sample 1 to sample 2) and decreasing the particle size from 100 nm to 50 nm (Table 4). Indeed, the R_{pol} value for the “isolated cauliflower” cathode (sample 1) was found to be 72.41 Ω.cm² at 700 °C whereas for the “connected round agglomerates” cathode (sample 2) 12.78 Ω.cm². In SOFC operation, the cathode is devoted to reducing the available oxygen molecules into oxygen ions, O²⁻, especially in the vicinity of triple phase boundary (TPB) points. Consequently, the electronic conductivity must be maximized and sufficient porosity is required to facilitate gas permeation. The microstructure of the cathode is therefore fundamental in enabling access of oxygen, electrons and ionic species between the cathode and the electrolyte, as well as expanding the number of TPB sites by increasing the total cathode surface area. For the 3-D coral-type microstructure the R_{pol} value is further reduced to 2.21 Ω.cm² at 700 °C (sample 3, Table 4) favored by a simultaneous improvement of the percolation path (Fig. 8g) and of the electrode/electrolyte contact (Fig. 8h), whereas the particle size is around 150 nm. This is believed to result from the increase in the number of contact points between the CGO substrate and the porous cathode layer due to the presence of the intermediate thin dense cathode layer. The beneficial impact of the addition of an interfacial layer at the electrode-electrolyte has also been previously reported in the literature.^{32,33} A decrease of the area specific resistance from 0.67 Ω.cm² to 0.21 Ω.cm² at 600°C was measured when 200 nm of La_{0.6}Sr_{0.4}Co_{0.2}Fe_{0.8}O_{3-δ} (LSCF) film was deposited on 3Y-TZP, (ZrO₂)_{0.97}(Y₂O₃)_{0.03}, electrolyte substrate by pulsed laser deposition (PLD) prior to the screen-printing of the porous LSCF cathode.³² In addition a decrease by 35% of the ASR was also reported using a La₂NiO_{4+δ} electrode when a dense thin electrode layer was added by PLD between the 3Y-TZP electrolyte and the screen-

printed porous electrode.³³ The presence of this layer is expected to improve the oxygen transfer towards the electrolyte.

It can be observed that by the addition of the $\text{La}_4\text{Ni}_3\text{O}_{10-\delta}$ current collecting layer (CCL) (sample 4) decreases the relative contribution of the *HF* response to the total electrode impedance. Indeed, for this double layer cathode, sample 4, only 1 arc is observed in the frequency range from 10 to 10^4 Hz in the plot (Fig. 9d). This is primarily caused by the total domination by R_{pol} (LF) and hence the low-frequency response of the sample 4 could be thought to be the rate-limiting step for this double layer cathode. On the other hand, a very small contribution at very low frequencies, appears at high temperatures (≥ 700 °C) and does not vary when the temperature is increased. Moreover the capacitance corresponding to this LF contribution is very high (of the order of 3.3 F.cm^{-2}), which suggests that it is related with bulk processes such as the O_2 diffusion in the gas phase.³⁴

A drastic improvement in the R_{pol} to a value as low as $0.30 \text{ } \Omega.\text{cm}^2$ at 700 °C (Fig.9d) has been measured when the 3-D coral-type microstructure was topped by a $\text{La}_4\text{Ni}_3\text{O}_{10-\delta}$ SP layer (Fig. 8). To the best of our knowledge this R_{pol} value is the lowest reported to date in the literature for $\text{La}_4\text{Ni}_3\text{O}_{10-\delta}$ cathode.³⁵ This double cathode is characterized by a porous cathode functional layer (CFL) with a fine particle size (~ 150 nm) of large surface area and good connectivity, as well as a good contact between the flat electrode surface (Fig. 8j) and the gold grid. In addition, this microstructure also possesses a good electrolyte/electrode contact (continuous thin and dense $\text{La}_4\text{Ni}_3\text{O}_{10-\delta}$ layer (Fig. 8l) improving the oxygen diffusion towards the electrolyte), as proved by the low R_s value. This decrease in R_{pol} of roughly ~ 7 times at 700 °C (16 times at 800 °C) in comparison to sample 3, can be attributed to the presence of a CCL which homogenizes the current distribution along the cathode functional layer (CFL), activating the whole volume of the cathode by avoiding any current constrictions and by increasing the lateral percolation. Remarkably, the R_{pol} obtained ($0.05 \text{ } \Omega \text{ cm}^2$ at 800 °C) of the double layer $\text{La}_4\text{Ni}_3\text{O}_{10-\delta}$ cathode developed here on an CGO electrolyte is lower than those for cathodes of the same composition reported elsewhere deposited by brush coating on LSGM and by screen-printing on YSZ electrolyte (1.0 and $0.15 \text{ } \Omega \text{ cm}^2$, respectively, at 800 °C).^{6, 36} The R_{pol} ($0.30 \text{ } \Omega \text{ cm}^2$ at 700 °C) also presents a better performance than those of the composite and functionally graded composite of $\text{La}_2\text{NiO}_{4+\delta}/\text{La}_4\text{Ni}_3\text{O}_{10-\delta}$ on a LSGM electrolyte at 700 °C (0.62 and $0.52 \text{ } \Omega \text{ cm}^2$, respectively)^{37, 38} and even lower than the CGO/ $\text{La}_4\text{Ni}_3\text{O}_{10-\delta}$ composite $0.435 \text{ } \Omega \text{ cm}^2$, at 700 °C.³⁹ As expected, R_{pol} decreases when the temperature increases (Fig.11, Table 4). The activation energies deduced from the Arrhenius plots (Fig. 11) are given in Table 4 and are in good agreement with the values reported in the literature.^{6, 36, 39} Our study highlights the importance of the microstructure in improving the cathode performance and puts this $\text{La}_4\text{Ni}_3\text{O}_{10-\delta}$ double layer microstructure as the best cathode reported to date for this composition.

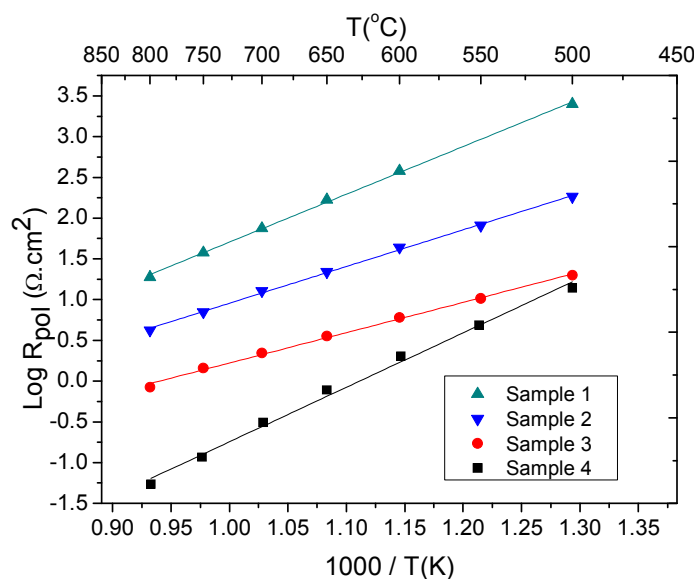


Fig. 11. Arrhenius plot of the R_{pol} in air for $\text{La}_4\text{Ni}_3\text{O}_{10-\delta}$ electrodes (OCP conditions) on CGO electrolyte, (a) sample 1, isolated cauliflower (b) sample 2, connected round agglomerates (c) sample 3, 3-D coral type (d) sample 4, double layer cathode (3-D coral type + SP).

4. Conclusions

This paper reports the fabrication of porous, continuous and crack-free $\text{La}_4\text{Ni}_3\text{O}_{10-\delta}$ cathodes on $\text{Ce}_{0.9}\text{Gd}_{0.1}\text{O}_{2-\delta}$ substrate by electrostatic spray deposition. Pure single phase $\text{La}_4\text{Ni}_3\text{O}_{10-\delta}$ films were obtained after calcination at 950 °C for 8 h in air, crystallizing in an orthorhombic symmetry. Various microstructures such as isolated cauliflowers, connected round agglomerates and 3-D coral-type films, have been obtained by optimizing the ESD key process parameters. Longer deposition times, favored preferential landing of the aerosol droplets and particle agglomeration. By increasing the substrate temperature and the nozzle to substrate distance, continuous and porous films can be obtained. The addition of 67% vol. water to pure ethanol gives a 3-D coral type microstructure with a continuous, dense thin layer adjacent to the electrolyte. It has been clearly shown that the electrochemical properties of these $\text{La}_4\text{Ni}_3\text{O}_{10-\delta}$ cathodes strongly depend upon the microstructure. R_{pol} improves from 74.94 to 12.78 and then to 2.21 $\Omega\cdot\text{cm}^2$ by changing the microstructure from isolated cauliflowers to connected round agglomerates and then to the 3-D coral-type microstructure, thanks to an improved percolation path and a better electrolyte/electrode contact. Moreover the R_{pol} value of the 3-D coral-type microstructure decreases down to 0.30 $\Omega\cdot\text{cm}^2$ at 700 °C after improving the current collection by adding a $\text{La}_4\text{Ni}_3\text{O}_{10-\delta}$ SP layer on top. To the best of our knowledge, this polarization resistance value is the lowest for this composition in the present literature.

Acknowledgments

This work was performed within the framework of the Centre of Excellence of Multifunctional Architected Materials "CEMAM" n° AN-10-LABX-44-01 funded by the "Investments for the Future" Program. The authors would like to thank S. Coindeau and T. Encinas for XRD and R. Martin for SEM and EDX analyses in CMTC (Grenoble INP, France). M.B. also acknowledges financial support from the Spanish Economy and Competitiveness Ministry through the "Juan de la Cierva" fellowship program.

References

- 1 J. H. Kim, M. Cassidy, J. T. S. Irvine and J. Bae, *Chem. Mater.*, 2010, **22**, 883.
- 2 G. Kim, S. Wang, A. J. Jacobson, L. Reimus, P. Brodersen and C. A. Mims, *J. Mater. Chem.*, 2007, **17**, 2500.
- 3 S. Park, S. Choi, J. Shin, and G. Kim, *RSC Adv.*, 2014, **4**, 1775.
- 4 J. A. Kilner and M. Burriel, *Annual Review of Materials Research*, 2014, **44**, 365
- 5 J.A. Kilner and C.K.M. Shaw, *Solid State Ionics*, 2002, **154**, 523.
- 6 G. Amow, I. J. Davidson, and S. J. Skinner, *Solid State Ionics*, 2006, **177**, 1205.
- 7 Z. Lou, J. Peng, N. Dai, J. Qiao, Y. Yan, Z. Wang, J. Wang and K. Sun, *Electrochemistry Communications*, 2012, **22**, 97.
- 8 S. Takahashi, S. Nishimoto, M. Matsuda and M. Miyake, *Journal of the American Ceramic Society*, 2010, **93**, 2329.
- 9 G. Amow and S.J. Skinner, *J. Solid State Electrochem.*, 2006, **10**, 538.
- 10 M. Burriel, G. Garcia, M. Rossell, A. Figueras, G. Van Tendeloo and J. Santiso, *Chem. Mater.*, 2007, **19**, 4056.
- 11 O. Wilhelm, S.E. Pratsinis, D. Perednis and L.J. Gauckler, *Thin Solid Films*, 2005, **479**, 121.
- 12 A. Wold and R.J. Arnott, *Journal of Physics and Chemistry of Solids*, 1959, **9**, 176.
- 13 A. Tarancón, M. Burriel, J. Santiso, S. J. Skinner and J.A. Kilner, *Journal of Materials Chemistry*, 2010, **20**, 3799.
- 14 R. Sayers, R.A. De Souza, J.A. Kilner and S.J. Skinner, *Solid State Ionics* 2010, **181**, 386
- 15 M.D. Carvalho, F.M.A. Costa, I.D.S. Pereira, A. Wattiaux, J.M. Bassat, J.C. Grenier and M. Pouchard, *J. Mater. Chem.*, 1997, **7**, 2107.
- 16 Z. Zhang and M. Greenblatt, *J Solid State Chem.* 1995, **117**, 236.
- 17 C.D. Ling, D.N. Argyriou, G. Wu and J.J. Neumeier, *J. Solid State Chem.*, 2000, **152**, 517.

- 18 X. Weng, P. Boldrin, I. Abrahams, S.J. Skinner and J.A. Darr, *Chem Mater.*, 2007, **19**, 4382.
- 19 C.H. Chen, M.H.J. Emond, E.M. Kelder, B. Meester and J. Schoonman, *J. Aerosol. Sci.*, 1999, **30**, 959.
- 20 R.C. Weast, *Handbook of Chemistry and Physics*, 56th edn., CRC Press, 1975, E-56.
- 21 D. Marinha, L. Dessemond and E. Djurado, *Current Inorganic Chemistry*, 2013, **3**, 2.
- 22 J. Rodriguez-Carvajal, *Phys. B*, 1993, **192**, 55.
- 23 J. F. Delamora and I.G. Loscertales, *J. Fluid Mech.*, 1994, **260**, 155.
- 24 O. Wilhelm, L. Madler and S.E. Pratsinis, *J. Aerosol Sci.*, 2003, **34**, 815.
- 25 A.M. Gañan-Calvo, J. Davila and A. Barrero, *J. Aerosol Sci.*, 1997, **28**, 249.
- 26 C.H. Chen, E.M. Kelder, P.J.J.M. van der Put and J. Schoonman, *J. Mater. Chem.*, 1996, **6**, 765.
- 27 B.-H. Hwang, C.-L. Chang, C.-S. Hsu and C.-Y. Fu, *J. Phys. D: Appl. Phys.*, 2007, **40**, 3448.
- 28 R. Neagu, D. Perednis, A. Princiville and E. Djurado, *Surf. Coat. Technol.*, 2006, **200**, 6815.
- 29 T. Nguyen and E. Djurado, *Solid State Ionics*, 2001, **138**, 191.
- 30 J. Sar, O. Celikbilek, J. Villanova, L. Dessemond, C. L. Martin and E. Djurado, *Journal of the European Ceramic Society*, 2015 (in press).
- 31 Adler SB, *Solid State Ionics*, 2000, **135**, 603.
- 32 N. Hildenbrand, B. A. Boukamp, P. Nammensma, D. H. A. Blank, *Solid State Ionics*, **192** (2011) 12.
- 33 N. Hildenbrand, P. Nammensma, D.H.A. Blank, H.J.M. Bouwmeester, B.A. Boukamp, *J. Power Sources*, **238** (2013) 442.
- 34 X. Xu, Z. Jiang, X. Fan and C. Xia, *Solid State Ionics*, 2006, **177** 2113.
- 35 C. Peter, A. Weber and E. Ivers-Tiffée, *Journal of the Electrochemical Society*, 2008, **155**, B730.
- 36 Z. Lou, N. Dai, Z. Wang, Y. Dai, Y. Yan, J. Qiao, J. Peng, J. Wang and K. Sun, *J Solid State Electrochem.*, 2013, **17**, 2703.
- 37 R. J. Woolley and S. J. Skinner, *Journal of Power Sources*, 2013, **243**, 790.
- 38 R. J. Woolley and S. J. Skinner, *Solid State Ionics*, 2014, **255**, 1.
- 39 S. Choi and G. Kim, *Journal of the Korean Ceramic Society*, 2014, **51**, 265.